Supporting information for: Identifying the Acceptor State in NiO Hole Collection Layers: Direct Observation of Exciton Dissociation and Interfacial Hole Transfer Across a Fe_2O_3/NiO Heterojunction

Somnath Biswas, Jakub Husek, Stephen Londo, Elizabeth A. Fugate, and L. Robert Baker*

Department of Chemistry and Biochemistry, The Ohio State University, Columbus, OH 43210

E-mail: baker.2364@osu.edu

Phone: +1 (614) - 292 - 2088

Contents

2. Ground State XUV-RA of Heterojunction

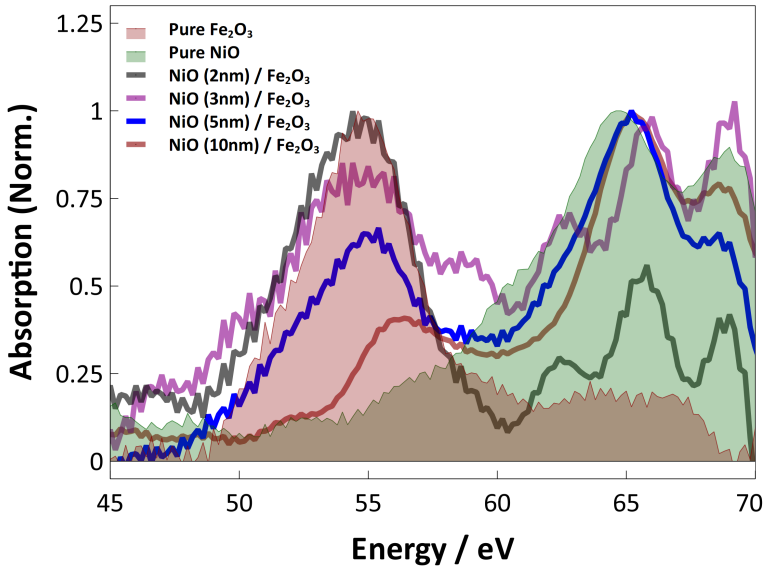

Figure S1: Ground State XUV-RA spectra of Fe_2O_3/NiO heterojunction as a function of NiO overlayer thickness. The shaded red and green background shows the ground state XUV-RA spectra of bulk Fe_2O_3 and NiO, respectively

The probe depth of XUV-RA measured at grazing incidence (8° relative to surface) as employed here is on the order of only 3 nm as previously reported.[S1] Consequently, the thickness of the NiO overlay should not be so thick to preclude measurement of the Fe $M_{2,3}$-edge from the Fe_2O_3 substrate through the NiO overlayer. Ground state spectra measured as a function of NiO overlayer thickness are shown in Figure S1, where these spectra are compared to that of a pure bulk NiO thin film. We observe that for very thin NiO overlayers, the Ni $M_{2,3}$-edge is spectrally different from the bulk NiO sample. This can be seen by the presence of a peak at 62.5 eV that is absent in the bulk sample, indicating the presence of Ni^+ defect states in very thin samples. As the average layer thickness is increased, the signature of Ni^+ defects disappears, and the Ni $M_{2,3}$-edge spectrum converges to that of the bulk NiO film.[S2] We take 5 nm as the thinnest NiO overlayer that has a spectrum which closely matches the bulk NiO reference sample. This sample represents a good experimental choice for transient measurements because the NiO film is sufficiently thin to enable measurement of exciton dynamics in the Fe_2O_3 substrate but is sufficiently thick to resemble nearly defect-

free NiO. The 5 nm thickness is assigned based on the NiO deposition rate measured using an in situ quartz crystal microbalance and represents an average thickness. We note that this average thickness of 5 nm is slightly greater than the nominal probe depth of this technique. As evidenced by electron miscroscopy, the SEM image for the heterojunction shows that majority of the surface largely resembles pure NiO Figure S3. However, additional sharp bright structures on the heterojunction surface are very similar to those present in pure Fe_2O_3, showing that the NiO overlayer does not form a continuous film atop the bulk Fe_2O_3 undelayer. Because of this inhomogeneity in the NiO overlayer, the spectral signature of the underlying Fe_2O_3 can be observed.

2. X-Ray Photoelectron Spectroscopy

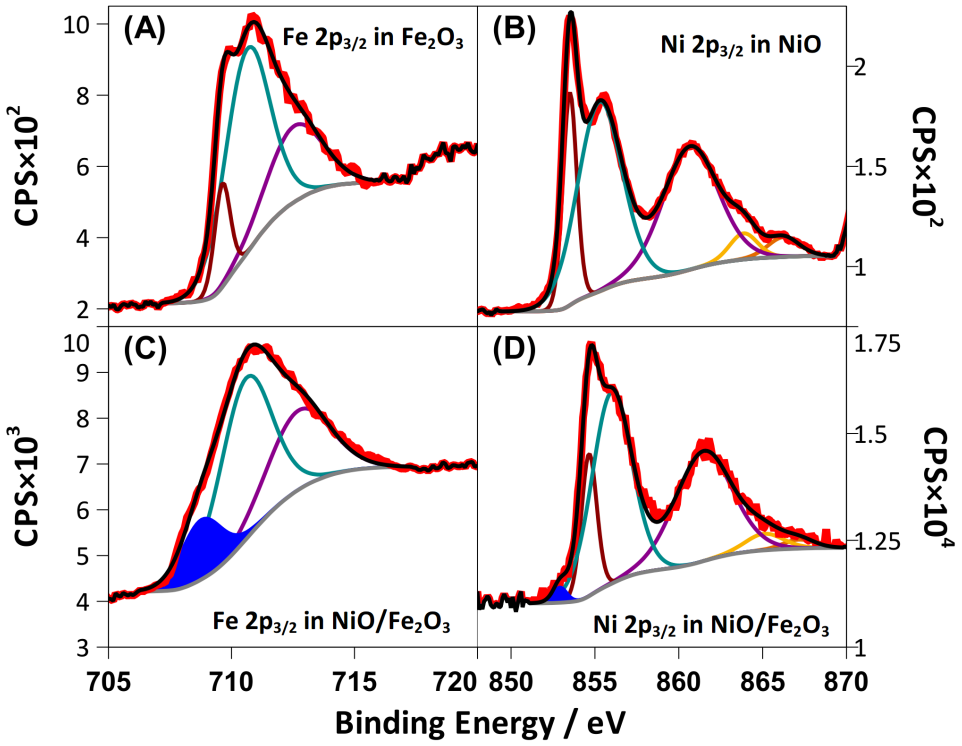

Figure S2: XPS spectra of (A) Fe $2p_{3/2}$ edge in Fe_2O_3 (B) Ni $2p_{3/2}$ edge in NiO (C) Fe $2p_{3/2}$ edge in Fe_2O_3/NiO(D) Ni $2p_{3/2}$ edge in Fe_2O_3/NiO. The shaded blue in C and D shows the partially reduced defect sites present in the heterojunction in the form of Fe^{2+} and Ni metal, respectively.

High resolution XPS analysis was performed to characterize all metal oxide samples using a Kratos Axis Ultra x-ray photoelectron spectrometer (monochromatic Al Kα X-ray source, E_{photon} = 1486.6 eV). The $2p_{3/2}$ transition was fit for all samples using Casa XPS software (Figure S2). All photoelectron spectra were referenced to adventitious carbon at 284.5 eV. Figure S2A and S2C compares the Fe $2p_{3/2}$ XPS multiplet structure in pure Fe_2O_3 and in Fe_2O_3/NiO heterojunction, respectively. Figure S2B and S2D compares the Ni $2p_{3/2}$ XPS multiplet structure in pure NiO and in Fe_2O_3/NiO heterojunction, respectively. From the fits of Fe_2O_3 (Figure S2A) and NiO (Figure S2B), we assign an oxidation state of 3+ to the iron center and +2 to the nickel center.[S3–S5]

We observe additional peaks in the heterojunction at 708.8 eV (Fe $2p_{3/2}$-edge) and 852.9

eV (Ni $2p_{3/2}$-edge), which are shaded in blue. The peak at 708.8 eV is associated with the reduced iron center (Fe^{2+}, 15.1%),[S6] while the peak at 852.9 eV is due to the presence of defect Ni metal sites (1.2%) at the interface of the Fe_2O_3/NiO heterojunction.[S7,S8] The interfacial hole transfer from Fe_2O_3 to the defect 3d states of Ni metal is observe by the appearance of a delayed weak excited state absorption at the Ni $M_{2,3}$-edge (63.6 eV) as described in the main manuscript.

Table S1: XPS fitting parameters for the data presented in Figure S2. The lettering in the column 1 directly corresponds to the lettering given in Figure S2, and the peak numbering is given from the highest energy peak to the lowest. All positions and widths are tabulated in units of eV.

	Peak 1			Peak 2			Peak 3			Peak 4			Peak 5			Peak 6		
	Position	Width	%	Position	Width	%	Position	Width	%	Position	Width	%	Position	Width	%	Position	Width	%
(A)	712.6	2.7	28.0	710.6	2.2	61.1	709.6	0.8	10.8	-	-	-	-	-	-	-	-	-
(B)	866.2	2.2	3.2	863.6	2.0	3.7	860.7	3.9	34.5	855.3	3.1	43.3	853.5	1.0	15.1	-	-	-
(C)	712.7	2.9	31.5	710.6	2.2	53.0	708.8	2.0	15.5	-	-	-	-	-	-	-	-	-
(D)	867.2	2.2	1.6	865.1	2.7	3.6	861.5	3.9	36.3	856.0	2.8	44.4	854.7	1.1	12.9	852.9	0.9	1.2

3. Scanning Electron Microscopy

The SEM images were measured using a Carl Zeiss Ultra 55 Plus Field-Emission Scanning Electron Microscope. The resulting images for Fe_2O_3, NiO, and Fe_2O_3/NiO heterojunction at low (A, B, C) and high (D, E, F) magnification, respectively, are shown in Figure S3. The SEM image for the heterojunction shows that majority of the surface largely resembles pure NiO, confirming the presence of the NiO overlayer. However, the sharp bright structures present on the heterojunction surface are very similar to those present in pure Fe_2O_3, suggesting that the NiO overlayer does not form a continuous film atop the bulk Fe_2O_3 underlayer.

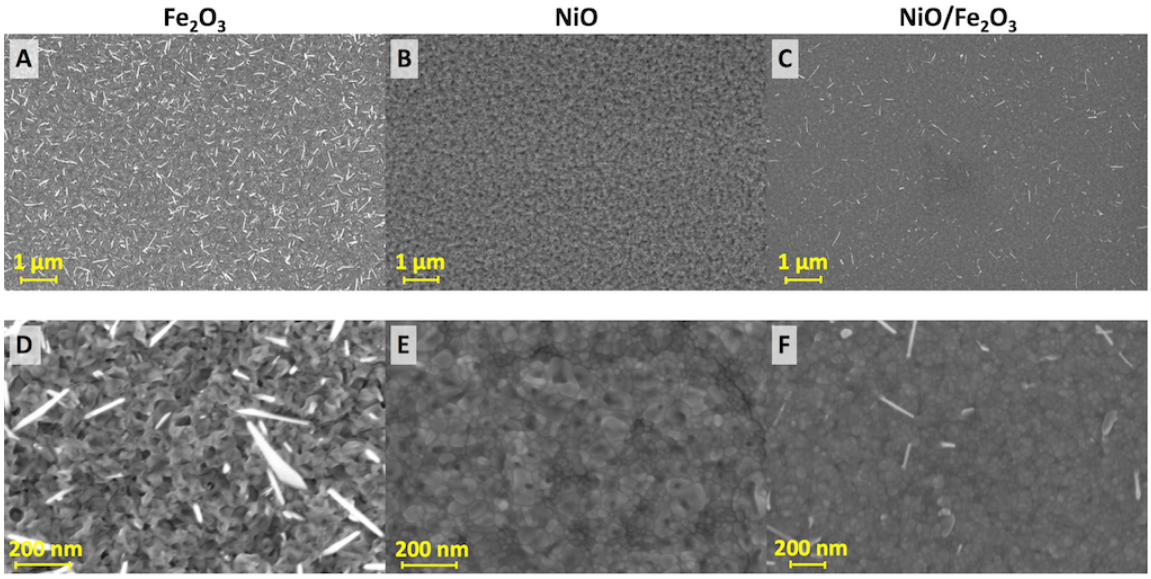

Figure S3: SEM images at low/high magnification for (A/D) Fe_2O_3, (B/E) NiO, (C/F) Fe_2O_3/NiO, respectively.

4. Atomic Force Microscopy

A Bruker AXS Dimension Icon Atomic/Magnetic Force Microscope with ScanAsyst, equipped with a TESPA-V2 cantilever, operating in tapping mode was used to measure the surface roughness for all metal oxide films. All images were recorded at a resolution of 512 samples/line with a 1.00 Hz scan rate and a scan area of 10x10 μm^2. The resulting images are shown in Figure S4 for Fe_2O_3, NiO, and $NiOFe_2O_3$. The root-mean-square surface roughness (R_q) for each sample is given in the figure caption, and was calculated using the NanoScope Analysis data processing software by Bruker.

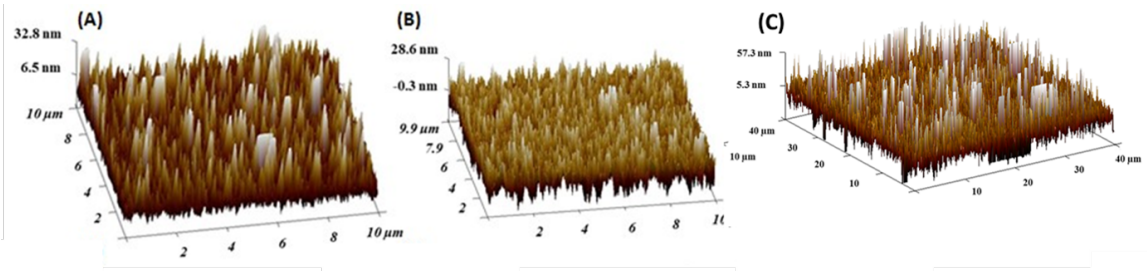

Figure S4: AFM images for (A) Fe_2O_3 ($R_q = 10$ nm), (B) NiO ($R_q = 16$ nm), (C) Fe_2O_3/NiO ($R_q = 12$ nm)

The root-mean-square surface roughness (R_q) for each sample is given in the figure caption, and was calculated using the NanoScope Analysis data processing software by Bruker.

5. Comparison of the Initial and Final State in Pure Fe_2O_3 and in Fe_2O_3/NiO Heterojunction

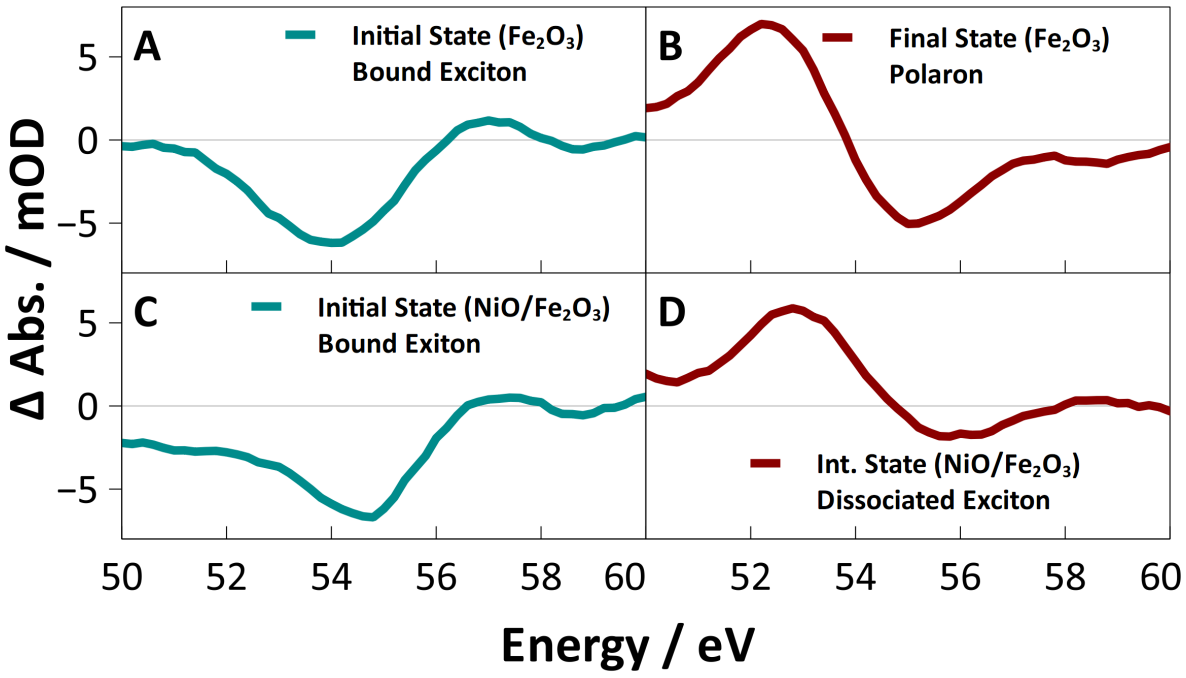

Figure S5: (A,B) Initial and final excited state of pure Fe_2O_3 photoexcited at 400 nm. (C,D) Initial and intermediate excited state of Fe_2O_3/NiO heterojunction photoexcited at 400 nm.

Performing a global fit to a two-state, sequential model for pure Fe_2O_3 produces initial and final state spectral vectors, which are analogous to those reported for the Fe_2O_3/NiO heterojunction in Figure 3C of the main manuscript. Here we compare the initial and final excited states obtained from pure Fe_2O_3 (Figure S5A, B) with the initial and intermediate excited states for the Fe_2O_3/NiO heterojunction sample (Figure S5C, D). We note that the heterostructure spectra have been fit to a three-state model, which accounts for the hole transfer to the NiO layer, while a two-state model is sufficient to describe the spectral evolution in pure Fe_2O_3. Consequently, the Fe_2O_3/NiO intermediate state is analogous to the Fe_2O_3 final state, which both reflect the time evolution at the Fe $M_{2,3}$-edge for these two samples. As shown, the initial excited state spectrum of the heterojunction sample closely matches with the initial excited state of the pure Fe_2O_3, which represents the signature of the

bound exciton as described in the main manuscript. However, the spectral signature of the intermediate state in heterojunction sample is different between the two samples, where the bleach feature at 55 eV recovers in the Fe_2O_3/NiO heterojunction sample. In contrast, this bleach persists for >100 ps with no sign of decay in the case of pure Fe_2O_3. As described in the main manuscript we assign this intermediate state in Fe_2O_3/NiO to exciton dissociation due to the presence of interface potential in the heterojunction sample.

6. Deconvolution of Polaron and Dissociated Exciton Formation

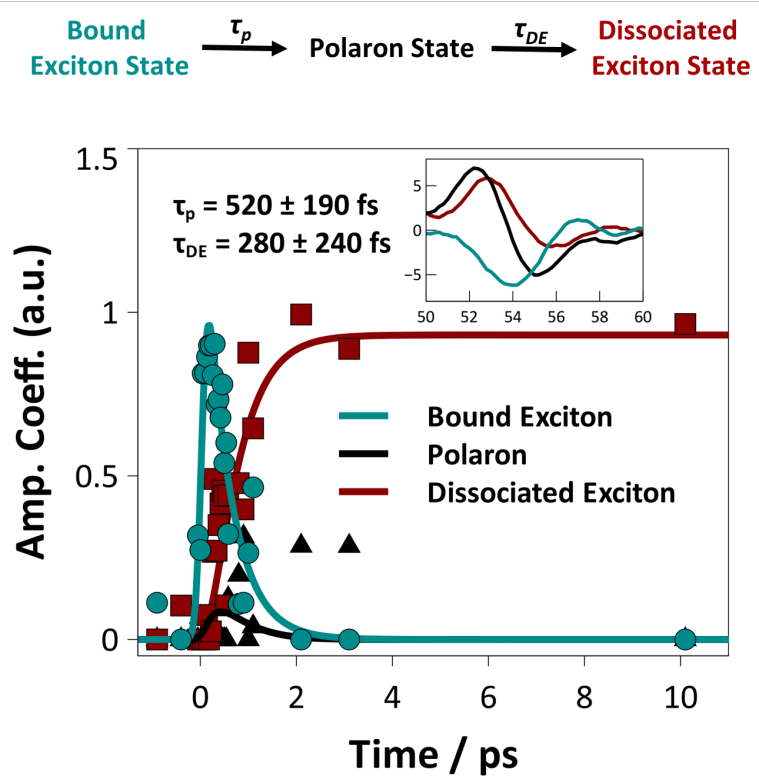

Figure S6: Schematic of the elementary steps for the formation of dissociated exciton. The amplitude coefficients of the initial bound exciton state, polaron state and dissociated exciton state in Fe_2O_3/NiO have been extracted from the respective vectors shown in the inset. The solid line shows fit to the experimental data assuming a sequential two-step kinetic process.

In previous work, we reported the time scale of bound exciton to the polaron formation at a Fe_2O_3 surface as $\tau_p = 640 \pm 20$ fs.[S9] In the case of the Fe_2O_3/NiO heterojunction, global kinetic analysis shows that bound exciton evolves to a dissociated exciton state with a time constant $(1/k_1)$ of 680 $\pm$ 60 fs. As described in the main manuscript this is an effective time constant for exciton dissociation, where the actual elementary step for dissociation is convoluted with small polaron formation in the Fe_2O_3 layer. In Fe_2O_3 polaron formation can be described as the expansion of the oxide lattice around the Fe^{2+} photoexcited metal center. Because electron density localizes on the Fe center and hole density localizes on the

O ligands, this lattice expansion serves to increase the exciton bond length and facilitate fast exciton dissociation. In an attempt to deconvolute the elementary polaron formation rate from the exciton dissociation rate in the heterojunction sample, we take the final state of pure Fe_2O_3 as a spectral signature of the polaron state and the initial and intermediate states of Fe_2O_3/NiO as the spectral signatures of the bound and dissociated exciton states, respectively. Subsequently, we calculate the time-dependent amplitude coefficients of the bound exciton, polaron and dissociated exciton state from the transient spectra of the Fe_2O_3/NiO heterojunction as shown in Figure S6. The associated vectors corresponding to the bound exciton state (cyan), polaron state (Black) and dissociated exciton (dark red) state are shown as an inset in Figure S6. The solid lines in Figure S6 show the fit to the experimental amplitude coefficients assuming a sequential two-step kinetic model where polaron formation precedes excitation dissociation. Results of the kinetic model indicate that small polaron formation occurs with a time constant of 520 $\pm$ 190 fs and that exciton dissociation occurs with a time constant of 280 $\pm$ 240 fs. We note that the amplitude coefficient of the polaron state is small compared to the bound or dissociated exciton states, showing that the exciton dissociation is fast relative to polaron formation. This analysis appears to confirm that exciton dissociation is strongly coupled to the lattice motion involved in bond elongation during the small polaron formation process in the presence of an interfacial electric field.

7. Kinetic Model

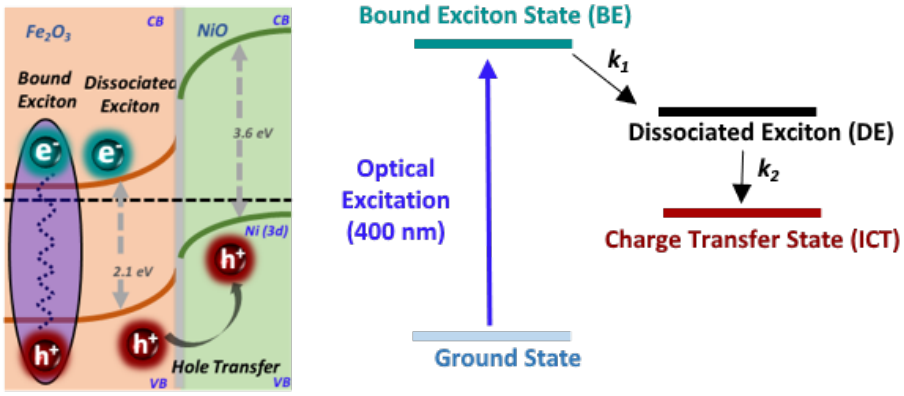

Figure S7: Two-step sequential kinetic model for field driven exciton dissociation with a rate constant of k_1 and subsequent interfacial hole transfer process with a rate constant of k_2

We find that the hole transfer occurs via the case 1 (Figure S7A) mechanism, where the interfacial electric field in the depletion region is sufficiently strong to drive exciton dissociation, and charge transfer occurs by subsequent drift of the minority carrier across the interface. Consequently, we utilize a sequential two-step kinetic model to describe this interfacial hole transfer process, where three distinct states evolve sequentially in the time domain, namely a bound exciton state (BE), a dissociated exciton state (DE), and an interfacial charge transfer state (ICT) as shown in Figure S7B. The field driven dissociation of BE state to the DE state occurs with a rate constant of k_1, while the subsequent formation rate of ICT state is k_2.

The following system of differential rate equations represent the rate of change of population for BE, DE, and ICT state.

$$\frac{d[BE]}{dt} = -k_1[BE] \tag{1}$$

$$\frac{d[DE]}{dt} = k_1[BE] - k_2[DE] \tag{2}$$

$$\frac{d[ICT]}{dt} = k_2[DE] \tag{3}$$

By integrating this system of differential rate equations we obtained the integrated rate equations for the population of BE, DE, and ICT.

$$[BE] = [BE]_0 e^{-k_1 t} \tag{4}$$

$$[DE] = \frac{k_1[BE]_0}{k_2 - k_1}\left(e^{-k_1 t} - e^{-k_2 t}\right) \tag{5}$$

$$[ICT] = [BE]_0\left(1 - \frac{1}{k_2 - k_1}(k_2 e^{-k_1 t} - k_1 e^{-k_2 t})\right) \tag{6}$$

However, experimental data is always convoluted with the instrument response function. Consequently, we have convoluted the expression of $[BE]$, $[DE]$, and [ICT] with a Gaussian function for a proper quantitative analysis of the data. The following shows the convolution of $[BE]$, $[DE]$, and [ICT] with a Gaussian instrument response of width σ and position t_0. In the fitting of these equations, σ is fixed at 100 fs, and t_0 is fixed at zero.

$$[BE] = \int_0^\infty [BE]_0 e^{-k_1 t} e^{-\frac{(t-t_0)^2}{2\sigma^2}} dt \tag{7}$$

$$[BE] = \frac{[BE]_0}{2} e^{-k_1\left(t - t_0 - \frac{\sigma^2 k_1}{2}\right)}\left[1 - erf\left(\frac{-t + t_0 + \sigma^2 k_1}{\sqrt{2}\sigma}\right)\right] \tag{8}$$

$$[DE] = \int_0^\infty \frac{k_1[BE]_0}{k_2 - k_1}\left(e^{-k_1 t} - e^{-k_2 t}\right) e^{-\frac{(t-t_0)^2}{2\sigma^2}} dt \tag{9}$$

$$\begin{aligned}[DE] = \frac{k_1[BE]_0}{k_2 - k_1}\left[\frac{1}{2} e^{-k_1\left(t - t_0 - \frac{\sigma^2 k_1}{2}\right)}\left[1 - erf\left(\frac{-t + t_0 + \sigma^2 k_1}{\sqrt{2}\sigma}\right)\right]\right] - \\ \frac{k_1[BE]_0}{k_2 - k_1}\left[\frac{1}{2} e^{-k_2\left(t - t_0 - \frac{\sigma^2 k_2}{2}\right)}\left[1 - erf\left(\frac{-t + t_0 + \sigma^2 k_2}{\sqrt{2}\sigma}\right)\right]\right]\end{aligned} \tag{10}$$

$$[ICT] = \int_0^\infty [BE]_0\left(1 - \frac{1}{k_2 - k_1}(k_2 e^{-k_1 t} - k_1 e^{-k_2 t})\right) e^{-\frac{(t-t_0)^2}{2\sigma^2}} dt \tag{11}$$

$$[ICT] = \frac{[BE]_0}{2}\left[1 - erf\left(\frac{-t+t_0}{\sqrt{2}\sigma}\right)\right] - \frac{k_2[BE]_0}{k_2-k_1}\left[\frac{1}{2}e^{-k_1\left(t-t_0-\frac{\sigma^2 k_1}{2}\right)}\left[1 - erf\left(\frac{-t+t_0+\sigma^2 k_1}{\sqrt{2}\sigma}\right)\right]\right] + \frac{k_1[BE]_0}{k_2-k_1}\left[\frac{1}{2}e^{-k_2\left(t-t_0-\frac{\sigma^2 k_2}{2}\right)}\left[1 - erf\left(\frac{-t+t_0+\sigma^2 k_2}{\sqrt{2}\sigma}\right)\right]\right] \quad (12)$$

As described in the main manuscript, the differential absorption intensity at 55 eV is associated with the population of BE state, and the combined differential absorption intensity at 65.6 eV and 68 eV are associated with the population of the ICT state. Therefore, the intensity of BE and ICT state has been fitted with equation 8 and 12, respectively. We obtain the field driven exciton dissociation rate, k_1 and hole transfer rate, k_2 from these fits. Accordingly, we calculate the population of DE from equation 10 as shown in Figure 4B in the main manuscript.

8. Transient XUV-RA Spectra

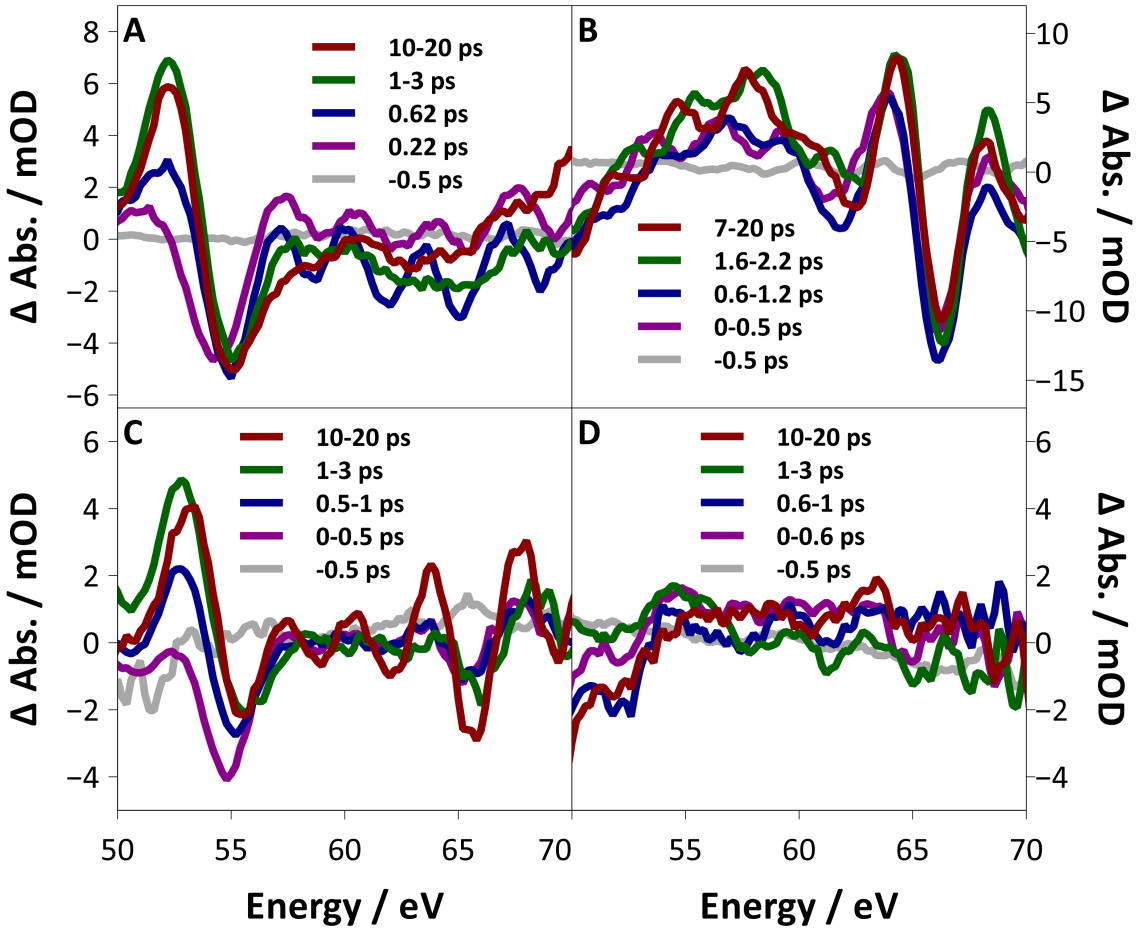

Figure S8: Transient XUV-RA spectra measured for pure Fe_2O_3 pumped at 400 nm (A), pure NiO pumped at 267 nm (B), the Fe_2O_3/NiO heterojunction pumped at 400 nm (C), and pure NiO pumped at 400 nm (D). For clarity these spectra have been averaged in the time domain as noted. These spectra were used to produce the contour plots shown in Figure 2 of the main manuscript.

9. Calculation of Interface Potential

Electric field can be obtained using the Gauss law of electrostatics.

$$E(x) = \frac{1}{\epsilon} \int \rho_{net}(x) dx \tag{13}$$

Considering that the depletion region has an abrupt charge distribution (e.g a step function) such that

$$\rho_{net} = -eN_A \qquad for - w_p < x < 0 \tag{14}$$

$$\rho_{net} = eN_D \qquad for \quad 0 < x < w_n \tag{15}$$

where e is the charge of electron, N_A and N_D are the carrier density in the p and n-side, respectively, and w_p and w_n are the width of the depletion region in the p and n-side, respectively, the electric field can be given as

$$E(x) = \frac{-eN_A}{\epsilon}(x + w_p) \qquad for - w_p < x < 0 \tag{16}$$

$$E(x) = \frac{eN_D}{\epsilon}(x - w_n) \qquad for \quad 0 < x < w_n \tag{17}$$

In this case, exciton dissociation happens at the n-side (Fe_2O_3) of the interface. The electric field is related to the potential by Equation 18

$$E(x) = -\frac{dV}{dx} \tag{18}$$

Integrating equation 18 gives the relation between the contact potential (V), the electric field (E) as a function of x, and the depletion width (w_n).

$$V(x) = \frac{eN_D}{2\epsilon}(x - w_n)^2 \tag{19}$$

The built-in potential in Fe_2O_3/NiO heterojunction is the difference between Fermi levels, $V = 1.4$ eV.[S10] Here we calculate the maximum electric field strength (E) at $x = 0$. Using the charge of an electron (1.6×10^{-19} C), the dielectric constant of Fe_2O_3 ($\epsilon = 1.24 \times 10^{-11}$ F/m), and the carrier density ($N_D \sim 10^{21}$ m^{-3}),[S11,S12] we estimate the depletion width, w_n = 0.47 μm, using Equation 19. From this the interfacial electric field is estimated to be 6.01 $\times 10^6$ V/m using Equation 17.

10. Comparison of Exciton Dissociation Probability

Field-induced exciton dissociation can be thought of as a tunneling process having a rate, which is proportional to the dissociation probability (P) given by

$$P \propto exp\left(-\frac{E_b}{edF_m}\right) \tag{20}$$

where E_b is exciton binding energy, e is elementary charge, d is exciton diameter, and F_m is electric field at the interface.[S13] Table S2 compares the tunneling probability in MoS_2 and Fe_2O_3 assuming similar exciton diameters of ∼1 nm in these two materials.

Table S2: Summary of Exciton Binding Energy, Electric Field Strength and Exciton Dissociation Probability in MoS_2 and Fe_2O_3

Material	E_b/eV	d/nm	F_m/(V/m)	P
MoS_2	0.5[S14]	1.0	1.0×10^{8}[S14]	6.7×10^{-3}
Fe_2O_3	0.04[S15]	1.0	1.0×10^{6}	1.3×10^{-3}

References

(S1) Cirri, A.; Husek, J.; Biswas, S.; Baker, L. R. *J. Phys. Chem. C* **2017**, *121*, 15861–15869.

(S2) Chen, H.-L.; Lu, Y.-M.; Hwang, W.-S. *Mater. Trans.* **2005**, *46*, 872–879.

(S3) Droubay, T.; Chambers, S. A. *Phys. Rev. B* **2001**, *64*, 205414.

(S4) Biesinger, M. C.; Payne, B. P.; Grosvenor, A. P.; Lau, L. W.; Gerson, A. R.; Smart, R. S. C. *Appl. Surf. Sci.* **2011**, *257*, 2717–2730.

(S5) Biesinger, M. C.; Payne, B. P.; Lau, L. W.; Gerson, A.; Smart, R. S. C. *Surf. Interface Anal.* **2009**, *41*, 324–332.

(S6) Yamashita, T.; Hayes, P. *Appl. Surf. Sci.* **2008**, *254*, 2441–2449.

(S7) Grosvenor, A. P.; Biesinger, M. C.; Smart, R. S. C.; McIntyre, N. S. *Surf. Sci.* **2006**, *600*, 1771–1779.

(S8) Gupta, P.; Dutta, T.; Mal, S.; Narayan, J. *J. Appl. Phys.* **2012**, *111*, 013706.

(S9) Husek, J.; Cirri, A.; Biswas, S.; Baker, L. R. *Chem. Sci.* **2017**, *8*, 8170–8178.

(S10) Wang, C.; Wang, T.; Wang, B.; Zhou, X.; Cheng, X.; Sun, P.; Zheng, J.; Lu, G. *Sci. Rep.* **2016**, *6*, 26432.

(S11) Mock, J.; Klingebiel, B.; Köhler, F.; Nuys, M.; Flohre, J.; Muthmann, S.; Kirchartz, T.; Carius, R. *Phys. Rev. Mater.* **2017**, *1*, 065407.

(S12) Hankin, A.; Alexander, J.; Kelsall, G. *Phys. Chem. Chem. Phys.* **2014**, *16*, 16176–16186.

(S13) Massicotte, M.; Vialla, F.; Schmidt, P.; Lundeberg, M. B.; Latini, S.; Haastrup, S.; Danovich, M.; Davydovskaya, D.; Watanabe, K.; Taniguchi, T. et al. *Nat. Commun.* **2018**, *9*, 1633.

(S14) Haastrup, S.; Latini, S.; Bolotin, K.; Thygesen, K. S. *arXiv preprint arXiv:1602.04044* **2016**,

(S15) Petit, S.; Melissen, S. T.; Duclaux, L.; Sougrati, M. T.; Le Bahers, T.; Sautet, P.; Dambournet, D.; Borkiewicz, O.; Laberty-Robert, C.; Durupthy, O. *J. Phys. Chem. C* **2016**, *120*, 24521–24532.